Compressible turbulent channel flow with impedance boundary conditions

Cite as: Phys. Fluids **27**, 035107 (2015); https://doi.org/10.1063/1.4914099
Submitted: 24 July 2014 . Accepted: 21 February 2015 . Published Online: 16 March 2015

Carlo Scalo, Julien Bodart, and Sanjiva K. Lele

PHYSICS OF FLUIDS **27**, 035107 (2015)

Compressible turbulent channel flow with impedance boundary conditions

Carlo Scalo,[1,a)] Julien Bodart,[2] and Sanjiva K. Lele[3]
[1]*Center for Turbulence Research, Stanford, California 94305-3024, USA*
[2]*Institut Supérieur de l'Aéronautique et de l'Espace (ISAE-Supaéro), Université de Toulouse, 31055 Toulouse, France*
[3]*Department of Aeronautics and Astronautics & Department of Mechanical Engineering Stanford, California 94305-4035, USA*

(Received 24 July 2014; accepted 21 February 2015; published online 16 March 2015)

We have performed large-eddy simulations of isothermal-wall compressible turbulent channel flow with linear acoustic impedance boundary conditions (IBCs) for the wall-normal velocity component and no-slip conditions for the tangential velocity components. Three bulk Mach numbers, $M_b = 0.05$, 0.2, 0.5, with a fixed bulk Reynolds number, $Re_b = 6900$, have been investigated. For each M_b, nine different combinations of IBC settings were tested, in addition to a reference case with impermeable walls, resulting in a total of 30 simulations. The adopted numerical coupling strategy allows for a spatially and temporally consistent imposition of physically realizable IBCs in a fully explicit compressible Navier-Stokes solver. The IBCs are formulated in the time domain according to Fung and Ju ["Time-domain impedance boundary conditions for computational acoustics and aeroacoustics," Int. J. Comput. Fluid Dyn. **18**(6), 503–511 (2004)]. The impedance adopted is a three-parameter damped Helmholtz oscillator with resonant angular frequency, ω_r, tuned to the characteristic time scale of the large energy-containing eddies. The tuning condition, which reads $\omega_r = 2\pi M_b$ (normalized with the speed of sound and channel half-width), reduces the IBCs' free parameters to two: the damping ratio, ζ, and the resistance, R, which have been varied independently with values, $\zeta = 0.5, 0.7$, 0.9, and $R = 0.01$, 0.10, 1.00, for each M_b. The application of the tuned IBCs results in a drag increase up to 300% for $M_b = 0.5$ and $R = 0.01$. It is shown that for tuned IBCs, the resistance, R, acts as the inverse of the wall-permeability and that varying the damping ratio, ζ, has a secondary effect on the flow response. Typical buffer-layer turbulent structures are completely suppressed by the application of tuned IBCs. A new *resonance buffer layer* is established characterized by large spanwise-coherent Kelvin-Helmholtz rollers, with a well-defined streamwise wavelength λ_x, traveling downstream with advection velocity $c_x = \lambda_x M_b$. They are the effect of intense hydro-acoustic instabilities resulting from the interaction of high-amplitude wall-normal wave propagation (at the tuned frequency $f_r = \omega_r/2\pi = M_b$) with the background mean velocity gradient. The resonance buffer layer is confined near the wall by structurally unaltered outer-layer turbulence. Results suggest that the application of hydrodynamically tuned resonant porous surfaces can be effectively employed in achieving flow control. © *2015 AIP Publishing LLC.* [http://dx.doi.org/10.1063/1.4914099]

I. INTRODUCTION

In low-speed boundary layers, acoustic perturbations are evanescent wave modes. As compressibility effects become more important, wave energy can amount to a sensible portion of the overall

a)Author to whom correspondence should be addressed. Electronic mail: scalo@purdue.edu. Present address: Department of Mechanical Engineering, Purdue University, West Lafayette, Indiana 47907-2045, USA.

fluctuating energy, with the potential to significantly affect the flow dynamics. In the present work, we explore this idea in the context of compressible wall-bounded turbulence control by manipulating the reflection of waves at the wall via the imposition of linear acoustic impedance boundary conditions (IBCs),

$$\hat{p} = Z(\omega)\hat{v}, \tag{1}$$

where $\hat{p}$ and $\hat{v}$ are the complex pressure and wall-normal velocity amplitudes, and $Z(\omega)$ is the acoustic impedance. Quantities in (1) are normalized with the speed of sound and density of the base flow (unitary reference impedance). The wall-normal velocity is positive if directed away from the flow domain. The time harmonic behavior $e^{i\omega t}$ is assumed where ω is the angular frequency.

Our approach relies on purely numerical predictions based on high-fidelity fully compressible three-dimensional turbulent simulations, warranting a robust and accurate time-domain formulation of impedance boundary conditions (TDIBCs). TDIBCs require several constrains to be met, which include causality and representation of the boundary as a passive element.[2] Many physically admissible impedance models have been proposed, with companion strategies for the time-domain formulation. Notable examples include the extended Helmholtz resonator model,[3] the z-transform method,[4,5] and the three-parameter model.[6] Additional challenges are present in their practical numerical implementation, especially when representing external boundaries.[7] A mathematically rigorous and effective approach is provided by Fung and Ju,[1] who proposed to apply IBCs indirectly via the reflection coefficient, with special care required in ensuring that the causality constraint is met. Fung and Ju[1]'s strategy has been adopted in the present work and is discussed in detail in the following.

The interaction between a boundary layer and wall-impedance is a classic problem in aeroacoustics. Numerous theoretical investigations by Rienstra and co-workers,[2,8–10] together with some companion experimental efforts,[11] have looked at the stability properties of boundary layers over homogeneous IBCs. In particular, the presence of hydro-acoustic instabilities was predicted under specific conditions, which were deemed to be rarely found in aeronautical practice. Such instability occurs when wall-normal acoustic wave propagation (controlled by the IBCs) becomes hydrodynamically significant. This type of instability has been reproduced in the present work in a fully developed compressible turbulent flow by *tuning* the characteristic resonant frequency of a mass-spring-damper model for the IBCs (a damped Helmholtz oscillator) to the characteristic hydrodynamic time scale of the flow. While the present results are purely numerical, experimental proof of concept of the proposed flow control strategy has already been successfully obtained in the context of laminar flow separation control over an airfoil by Yang and Spedding.[12]

Control of boundary layer turbulence and transition via modified wall-boundary conditions is a topic of formidable research effort. Bodony and co-workers[13,14] have investigated the interaction of a two-dimensional compressible boundary layer with a single wall-mounted Helmholtz cavity and of a supersonic turbulent boundary layer with a fluttering panel. Tam *et al.*[15] have simulated a laminar boundary layer developing over an array of resolved wall-mounted Helmholtz resonators. Particular interest is present in the hypersonic-transition community, where accurate characterization of acoustic properties of ultrasonic absorptive coatings (UAC) has shown to be crucial towards understanding their effects on transition control.[16] Bres *et al.*[17] investigated the stability properties of a two-dimensional hypersonic boundary layer over an idealized porous wall and adopted a simple impedance model for companion linear stability calculations. Various high-fidelity numerical simulations have been performed[18,19] looking at the interaction between a simplified porous wall geometry and supersonic boundary layers.

The same problem has been investigated in the incompressible limit with more focus on characterizing the structural alterations to wall-bounded turbulence. The interaction between an incompressible turbulent channel flow and a porous wall, for example, has been explored by Jiménez *et al.*[20] using Darcy-type wall boundary conditions. Large Kelvin-Helmholtz spanwise-coherent rollers were observed in the outer layer and found responsible for the increased frictional drag. The latter was associated with the wall shear stress increase in regions of suction, outweighing its decrease in regions of blowing, both modulated by the large outer layer rollers. The drag increase, therefore, did not result from the strengthening of the classic near-wall turbulence cycle,[21] which was not significantly altered.

Similar flow alterations were observed by Flores and Jiménez[22] who introduced a rough wall modeled via the direct imposition of non-zero Reynolds shear stresses at the boundary. This resulted in near-isotropic vortex clusters in the inner layer disrupting the near-wall turbulence production cycle. In this case, however, a negligible effect on the flow was observed when only wall-normal transpiration was allowed. Effects on the outer-layer structure are typically noticeable only for sufficiently large roughness heights,[23] consistently with Townsend's conjecture[24] stating that buffer layer dynamics can be perturbed without altering the outer flow. A similar conclusion is present in the analysis of a sink flow over a rough wall by Yuan and Piomelli[25] where a large roughness height causes decorrelation between the outer-layer vortex packets and the near-wall structures. A roughness sublayer can be identified, playing in rough-wall flows the same role of the smooth-wall buffer layer. As discussed in the following, the application of tuned wall-impedance conditions triggers intense hydro-acoustic instabilities, which are confined in a *resonance buffer layer*, with a very well-defined spatial-temporal structure, underlying unaltered outer-layer equilibrium turbulence.

Other modified wall surface geometries that are relevant to our study are spanwise-periodic and streamwise-ribbed wavy walls, such as the ones investigated by Henn and Sykes,[26] confirming the findings of numerous previous experiments performed in water channels.[27,28] Low-amplitude wavy walls (below the separation regime) cause the formation of large-scale turbulent motions composed of meandering streamwise structures with large spanwise and streamwise extents, enhancing mixing rates at the troughs while not affecting the viscous sublayer structure. Flows over ribbed surfaces have been the focus of numerous research efforts, with progressively refined experimental and numerical strategies. Among them, Garcia-Mayoral and Jiménez[29] analyzed the effect of the relaxation of the impermeability condition at a ribbed wall with riblets larger than the optimal size. In this regime, they reported spanwise rollers centered at $y^+ \approx 10 - 15$ above riblet tips and with streamwise wavelength of $\lambda_x^+ \approx 150$. They were attributed to an inviscid Kelvin-Helmholtz instability enhancing Reynolds shear stresses, which account for the drag increase past the breakdown of the viscous regime. The observed instability is merely hydrodynamic.

The present work investigates the interaction between a damped Helmholtz oscillator model, represented by a three-parameter broadband impedance,[6] and fully developed compressible channel flow turbulence. The goal is to analyze the alterations to the near-wall turbulent structure resulting from the application of tuned wall-impedance in flow configurations previously explored only with impermeable walls.[30–34] Relying on high-fidelity three-dimensional fully compressible Navier-Stokes simulations allows to fully capture the nonlinear interactions between wave fluctuations and hydrodynamic events, which characterize the observed flow instability. Moreover, the TDIBC implementation strategy adopted provides an exact representation of the acoustic response of a porous surface without the need to resolve its complex geometrical structure. To our knowledge, no previous study has outlined the details of the coupling between TDIBCs and a fully compressible Navier-Stokes solver or has analyzed the structure of a hydro-acoustic instability occurring within a fully developed turbulent flow. The simplicity, uniqueness, and relevance of the problem has motivated the present study.

In the following, we first explain the coupling strategy between a fully compressible explicit Navier-Stokes solver and IBCs. The governing equations and boundary conditions are then analyzed to identify an appropriate dimensionless parameter space to explore. Baseline results for a turbulent compressible channel flow are reproduced with IBCs acting as hard walls (i.e., in the limit of $|Z(\omega)| \to \infty$) and are validated against other numerical simulations available in the literature for isothermal (impermeable) walls. Finally, results from turbulent channel flow coupled with tuned IBCs are analyzed and compared to previous work.

II. TDIBC

In this section, the proposed coupling strategy between the time-domain formulation of impedance boundary conditions by Fung and Ju[1] and a fully explicit compressible Navier-Stokes solver is discussed, along with the details of the comparison with a semi-analytical solution. Some of the basic ideas outlined in Fung and Ju[1] are repeated for the sake of completeness. The normalization

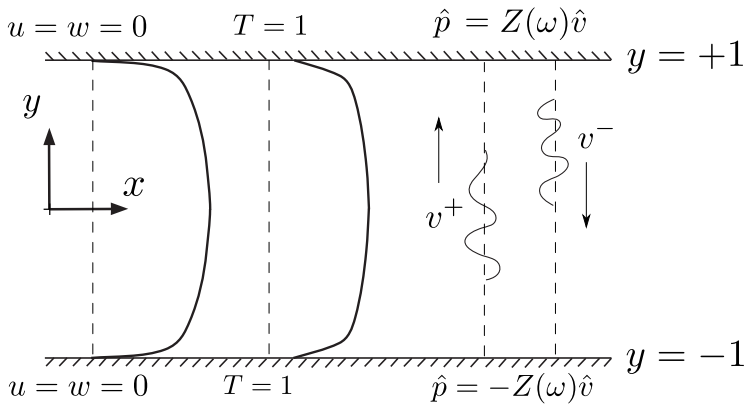

FIG. 1. Computational setup for LES of compressible turbulent channel flow with impedance boundary conditions interacting with up-traveling, v^+, and down-traveling v^- waves. All quantities shown are non-dimensionalized with the speed of sound based on the wall temperature, the wall-temperature itself and the channel half-width. The negative sign for the bottom-wall IBC is necessary to preserve symmetry (see velocity convention in (1)).

adopted is based on the base density and speed of sound, consistently with the scaling parameters used for the normalization of the channel flow large-eddy simulations (LES) calculations.

A. Coupling with a time-explicit Navier-Stokes solver

For the sake of consistency with the computational setup shown in Figure 1, this section will focus on planar-wave propagation in the wall-normal coordinate direction, y. Up- and down-traveling waves are, respectively, indicated as

$$\begin{cases} v^+ = v' + p', & \text{(2a)} \\ v^- = v' - p', & \text{(2b)} \end{cases}$$

where v' and p' are the fluctuating wall-normal velocity and pressure. The base density and speed of sound are omitted, being unitary in the normalization adopted.

Without loss of generality, hereafter, the discussion will be limited to the impedance condition at the upper wall, for which v^+ and v^- are, respectively, incident and outgoing waves. Substituting (1) into (2) yields

$$\hat{v}^-(\omega) = \widehat{W}(\omega)\,\hat{v}^+(\omega), \tag{3}$$

where $\widehat{W}(\omega)$ is the reflection coefficient, defined as

$$\widehat{W}(\omega) = \frac{1 - Z(\omega)}{1 + Z(\omega)}. \tag{4}$$

The relation between incident and outgoing waves can be alternatively expressed via the wall-softness, $\widehat{\widetilde{W}}(\omega)$,

$$\hat{v}^-(\omega) = -\hat{v}^+(\omega) + \widehat{\widetilde{W}}(\omega)\,\hat{v}^+(\omega), \tag{5}$$

where $\widehat{\widetilde{W}}(\omega) = \widehat{W}(\omega) + 1$ or $\widehat{\widetilde{W}}(\omega) = 2/(1 + Z(\omega))$.

Total reflection from a hard surface, $\hat{v} = 0$, corresponds to $\widehat{W}(\omega) = -1$ and $\widehat{\widetilde{W}} = 0$, while a pressure surface, $\hat{p} = 0$, corresponds to $\widehat{W}(\omega) = 1$ and $\widehat{\widetilde{W}}(\omega) = 2$. The reflection coefficient can be interpreted as a transfer function with $\hat{v}^+$ being the input signal and $\hat{v}^-$ the output.

Fung and Ju[1] have pointed out that, provided that all poles of $\widehat{\widetilde{W}}(\omega)$ (or zeros of $1 + Z(\omega)$) are located in the upper half of the complex ω-plane, the outgoing wave can be derived via causal

convolution of the incident wave,

$$v^-(t) = -v^+(t) + \int_0^\infty \widetilde{W}(\tau) v^+(t-\tau) d\tau. \tag{6}$$

Evaluating (6) at $t + \Delta t$, where Δt is a finite time interval (for example the Navier-Stokes solver's Runge-Kutta sub-time step), and applying the residue theorem to decompose the convolution integral on the right hand side, yields

$$v^-(t+\Delta t) = -v^+(t+\Delta t) + \sum_k v_k^-(t+\Delta t), \tag{7}$$

where the k-th contribution to the convolution integral can be expressed as

$$v_k^-(t+\Delta t) = \int_0^\infty \mu_k e^{i\lambda_k \tau} v^+(t+\Delta t-\tau) d\tau, \tag{8}$$

where μ_k is the k-th residue of $\widehat{\widetilde{W}}(\omega)$,

$$\mu_k = i \ \text{Residue}[\widehat{\widetilde{W}}(\omega), \lambda_k] \tag{9}$$

calculated for the pole λ_k. Invoking the internal addition property of the integral in (8), it can be shown that

$$v_k^-(t+\Delta t) = z_k v_k^-(t) + \int_0^{\Delta t} \mu_k e^{i\lambda_k \tau} v^+(t+\Delta t-\tau) d\tau, \tag{10}$$

where $z_k = e^{i\,\lambda_k \Delta t}$. Fung and Ju[1] have proposed to evaluate the integral in (10) with a trapezoidal quadrature rule (second-order accurate), yielding

$$v_k^-(t+\Delta t) = z_k v_k^-(t) + \mu_k \Delta t \left[w_{k0}\, v^+(t+\Delta t) + w_{k1}\, v^+(t) \right], \tag{11}$$

where

$$\begin{cases} w_{k0} = -\dfrac{z_k - 1}{\lambda_k^2 \Delta t^2} - \dfrac{1}{i\lambda_k \Delta t}, & \text{(12a)} \\ w_{k1} = \dfrac{z_k - 1}{\lambda_k^2 \Delta t^2} + \dfrac{z_k}{i\lambda_k \Delta t}. & \text{(12b)} \end{cases}$$

Relations (7) and (11) in their current form, however, do not provide a straightforward means to update the solution at the boundary in time, which is required in a Navier-Stokes solver. This is possible only if a prediction for $v^+(t+\Delta t)$ in (7) and (11)—future value at the boundary of the incoming wave—is provided. We propose to estimate the latter by extrapolating the value of the incoming wave in time based using the truncated Taylor series expansion in space,

$$v^+(t+\Delta t) \simeq p'(y-\Delta t, t) + v'(y-\Delta t, t) \simeq [p'(y,t) + v'(y,t)] - \Delta t \frac{\partial}{\partial y} [p'(y,t) + v'(y,t)], \tag{13}$$

evaluated at $y = +1$. The value of $v^+(t+\Delta t)$ in (13) is therefore predicted based on the values of pressure and velocity (and their gradients) at the boundary. The speed of sound is unitary in the currently adopted normalization and is therefore not explicitly present in (13). The fluctuating pressure and wall-normal velocity field at time $t + \Delta t$ are finally given by

$$\begin{cases} v'(t+\Delta t) = \dfrac{1}{2}\left[v^+(t+\Delta t) + v^-(t+\Delta t) \right], & \text{(14a)} \\ p'(t+\Delta t) = \dfrac{1}{2}\left[v^+(t+\Delta t) - v^-(t+\Delta t) \right] & \text{(14b)} \end{cases}$$

and are applied as Dirichlet boundary conditions for pressure and wall-normal velocity. No-slip conditions are enforced for the tangential components of the velocity and isothermal conditions for temperature, leading to the viscous momentum and conductive heat flux formulation typically adopted for isothermal walls.

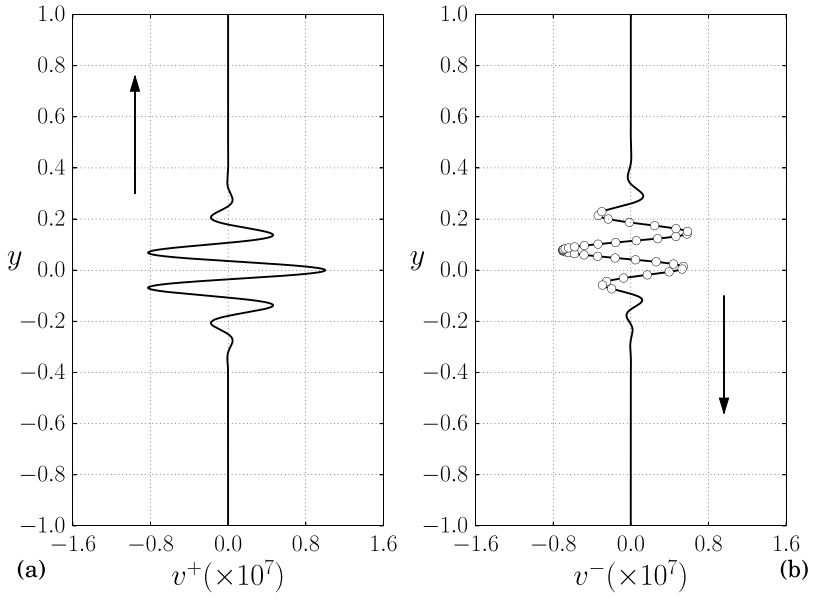

FIG. 2. Planar up-traveling wave (16) interacting with impedance boundary condition (15) at $y = +1$. Up-traveling wave (16) at $t = 0$ (a) and reflected, down-traveling wave (b) at $t = 2$. Numerical solution from Navier-Stokes solver (—) and semi-analytical solution (20) (∘). Arrow shows direction of propagation of the wave. Values of the parameters in (16) are: $A = 10^{-6}$, $\alpha = 0.8$, $k = 7$; values of the parameters in the IBCs (15) are: $R = 0.20$, $X_{-1} = 40$ rad, $X_{+1} = 2.5 \times 10^{-2}$ rad^{-1}.

B. Impedance tube test case

In the following, we provide the details of a one-dimensional impedance-tube test case for validation of the TDIBC implementation (Sec. II A) in the same fully compressible Navier-Stokes solver used for the turbulent channel flow calculations (Sec. III B). The test case consists of a plane-wave propagating in the y direction interacting with a damped Helmholtz oscillator,

$$Z(\omega) = R + i\left[\omega X_{+1} - \omega^{-1} X_{-1}\right], \tag{15}$$

at $y = +1$ (Figure 2) where R is the resistance and the X_{+1} and X_{-1} are the acoustic mass and stiffness, respectively, and ω is the angular frequency. All quantities in (15) are made dimensionless with the speed of sound (consistently with all the other sections of the paper) and a reference length scale set by the initial conditions, equal to the distance of the initial waveform peak from the impedance at $y = +1$ (i.e. the channel's half-width).

Building upon the semi-analytical solution proposed by Tam and Auriault,[6] let us consider the reflection of the broadband disturbance

$$\begin{cases} p'(y,t) = \dfrac{1}{2} A\, e^{-\alpha\, k^2 (y-t)^2} \cos\left[2\pi\, k\, (y-t)\right], & \text{(16a)} \\ v'(y,t) = p'(y,t) & \text{(16b)} \end{cases}$$

(purely up-traveling wave) where A, α, and k are dimensionless parameters defining, respectively, the wave form's amplitude, spatial support, and wavenumber. The instantaneous value of the up-traveling wave (2a) at $y = +1$ is

$$v^+_{y=1}(t) = 2\, p'(1,t) \tag{17}$$

and the value of the corresponding reflected wave at $y = +1$, $v^-_{y=1}(t)$, can be calculated by taking the inverse Fourier transform of (3),

$$v^-_{y=1}(\tau) = \frac{1}{2\pi} \int_{-\infty}^{+\infty} \widehat{W}(\omega) \hat{v}^+_{y=1}(\omega) e^{i\omega\,\tau} d\omega. \tag{18}$$

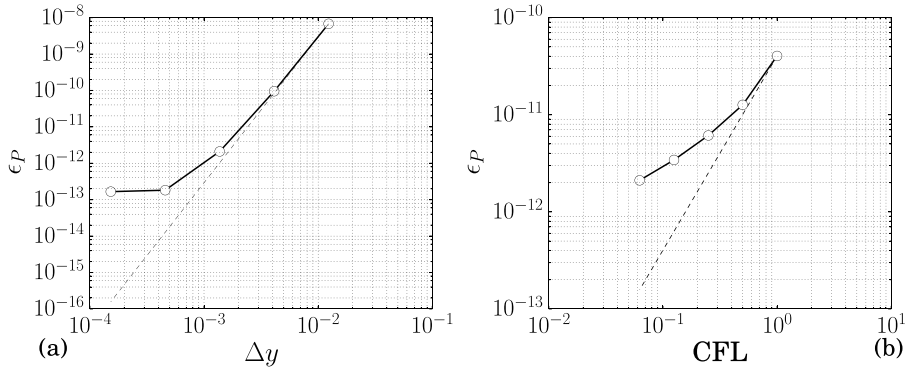

FIG. 3. Root-mean-square difference over the interval $-0.4 < y < 0.4$ between numerical solution at time $t = 2$ integrated from initial conditions (16) and semi-analytical solution (20) versus grid size Δy for CFL = 0.1 (a) and versus CFL for finest grid available (b), where CFL is the Courant–Friedrichs–Lewy number based on the speed of sound. Dashed lines showing fourth-order accuracy in space, Δy^{-4}, and second-order accuracy in time, CFL^{-2}. Numerical solutions in the time domain are obtained with prediction step (13).

The analytical expression for $\hat{v}^{+}_{y=1}(\omega)$ can be calculated based on the Fourier transform of $p'(1,t)$ in (16)

$$\hat{v}^{+}_{y=1}(\omega) = -e^{-i\omega}\frac{A}{2k}\sqrt{\frac{\pi}{\alpha}}\left[e^{-\frac{1}{4\alpha}\left(\frac{\omega}{k}+2\pi\right)^2} + e^{-\frac{1}{4\alpha}\left(\frac{\omega}{k}-2\pi\right)^2}\right]. \tag{19}$$

The reflected wave reconstructed in space and time, $v^{-}(y,t)$, is obtained assuming linear acoustic propagation of the outgoing wave,

$$v^{-}(y,t) = v^{-}_{y=1}(t-[1-y]). \tag{20}$$

Excellent agreeme nt is observed between (20), calculated via numerical integration of (18) in the frequency domain, and the solution from the Navier-Stokes solver (Figure 2). The root-mean-square (RMS) of the difference between the two solutions, evaluated over the interval $-0.4 < y < 0.4$ at $t = 2$, decays initially with fourth-order accuracy in space and second-order in time (Figure 3), as expected. Several trials have shown that this metric is very sensitive to the integration strategy adopted when carrying out complex indefinite integral (18). This is due to the nature of the integrand in (18) causing the accumulation of round–off error to become more severe (i.e., approaching the value of the integration result itself) as τ departs from unity, that is, for values of y departing from 0, at $t = 2$. Achieving convergence on (18) was therefore only possible by carrying out the numerical integration in the frequency domain to the maximum accuracy achievable. For values of y approximately $y < -0.2$ and $y > 0.2$, rapid accumulation of round-off error caused the iterative numerical quadrature procedure to halt before the desired accuracy was reached. These (and other) issues are responsible for the plateauing of the error (Figure 3). The prediction step (13) reduces the overall error by almost one order of magnitude (not shown), while not affecting the order of convergence. Overall, the quality of the adopted TDIBC formulation and of proposed coupling strategy with a Navier-Stokes solver are very satisfactory.

The focus on wall-normal planar wave propagation is sufficient to validate the implementation of the IBCs (1) given their intrinsic one-dimensional nature. Any other linear acoustic test case involving oblique wave reflection would be a linear superposition of two planar waves, one of which would propagate undisturbed in the direction parallel to the wall.

III. PROBLEM FORMULATION

A. Governing equations

In this section, we present the complete set of governing equations and boundary conditions to determine the appropriate dimensionless parameter space to explore. Hereafter, all reported quantities are non-dimensionalized with the speed of sound based on the wall temperature, the wall

temperature itself, the channel half-width, and bulk density (constant for channel-flow simulations) and are intended as filtered quantities.[35] The conservation of mass, momentum, and total energy reads

$$\begin{cases} \dfrac{\partial}{\partial t}\rho + \dfrac{\partial}{\partial x_j}\left(\rho u_j\right) = 0, & \text{(21a)} \\ \dfrac{\partial}{\partial t}\left(\rho u_i\right) + \dfrac{\partial}{\partial x_j}\left(\rho u_i u_j\right) = -\dfrac{\partial}{\partial x_i}p + \dfrac{1}{Re}\dfrac{\partial}{\partial x_j}\left(\tau_{ij}\right) + f_1(M_b)\,\delta_{1i}, & \text{(21b)} \\ \dfrac{\partial}{\partial t}\left(\rho E\right) + \dfrac{\partial}{\partial x_j}\left[u_j\left(\rho E + p\right)\right] = \dfrac{1}{Re}\dfrac{\partial}{\partial x_j}\left[u_i\,\tau_{ij} - q_j\right] + u_1\,f_1(M_b), & \text{(21c)} \end{cases}$$

where the gas is ideal with equation of state $p = \gamma^{-1}\rho T$, γ is the ratio of specific heats, and E is the total energy per unit mass. The viscous stress tensor and conductive heat fluxes, including the sub-grid scale (SGS) contributions, are, respectively,

$$\begin{cases} \tau_{ij} = 2\left(\mu + \mu_{sgs}\right)\left[S_{ij} - \dfrac{1}{3}\dfrac{\partial u_m}{\partial x_m}\delta_{ij}\right], & \text{(22a)} \\ q_j = -\left(\dfrac{\mu}{Pr} + \dfrac{\mu^{sgs}}{Pr^{sgs}}\right)\dfrac{\partial T}{\partial x_j}, & \text{(22b)} \end{cases}$$

where S_{ij} is the strain-rate tensor, μ the (molecular) dynamic viscosity, respectively, given by $S_{ij} = (1/2)\left(\partial u_j/\partial x_i + \partial u_i/\partial x_j\right)$ and $\mu = T^n$ where n is the viscosity exponent. The dynamic viscosity is normalized with its value at the wall, which corresponds to the reference value used in the Reynolds, Re, and, Prandtl, Pr, numbers. The subgrid scale contributions, labeled using the ^{sgs} superscript, are modeled according to the Vreman[36] sub-grid scale formulation. The subgrid-scale eddy viscosity is calculated as

$$\mu^{sgs} = \rho C^{Vr}\Delta_v^{2/3}\left(\frac{\beta_{11}\beta_{22} - \beta_{12}^2 + \beta_{11}\beta_{33} - \beta_{13}^2 + \beta_{22}\beta_{33} - \beta_{23}^2}{\alpha_{ij}\alpha_{ij}}\right)^{1/2}, \tag{23}$$

where $\alpha_{ij} = \partial u_j/\partial x_i$, $\beta_{ij} = \alpha_{mi}\alpha_{mj}$, and Δ_v is the cell volume. The constants C^{Vr} and Pr^{sgs} are set, respectively, to 0.07 and 0.9.

The body force f_1 in (21b) is only applied in the streamwise direction and dynamically adjusted at run-time to achieve the desired bulk Mach number, $M_b = \langle\rho u\rangle_{\mathcal{V}}/\langle\rho\rangle_{\mathcal{V}}$, where $\langle\cdot\rangle_{\mathcal{V}}$ is the volume-averaged operator.

The IBCs, no-slip conditions for the tangential velocities and the isothermal conditions,

$$\begin{cases} \hat{p} = \pm Z(\omega)\,\hat{v}, & \text{(24a)} \\ u = w = 0, & \text{(24b)} \\ T = 1, & \text{(24c)} \end{cases}$$

respectively, are applied at the walls, $y = \pm 1$, with impedance $Z(\omega)$ is given by (15). For a given value of the resistance R, the acoustic mass, X_{+1}, and stiffness, X_{-1}, can be expressed as a function of undamped resonant angular frequency, ω_r, and damping ratio, ζ, where

$$\begin{cases} \omega_r = \sqrt{\dfrac{X_{-1}}{X_{+1}}}, & \text{(25a)} \\ \zeta = \dfrac{1+R}{2\,\omega_r\,X_{+1}}. & \text{(25b)} \end{cases}$$

It can be shown that damping ratios higher than 1 lead to inadmissible (or anti-causal) impedance, violating the assumption underlying (6), and, therefore, cannot be considered. For a given value of the resistance R, the relations in (25) establish a one-to-one correspondence between the sets of parameters $\{R, X_{-1}, X_{+1}\}$ in (15) and $\{R, \omega_r, \zeta\}$. The latter will be the set of choice for the following analysis.

By choosing $Pr = 0.72$, $n = 0.76$, and $\gamma = 1.4$, valid for air,[37] five dimensionless parameters are left characterizing the fully coupled problem: two in the governing flow equations, Re, based on the speed of sound, and M_b, and three in the IBCs in the set $\{R, \omega_r, \zeta\}$. The Reynolds number based on the bulk velocity, Re_b, is not an independent parameter, since $Re_b = Re\,M_b$.

B. Computational setup

The aforementioned dimensionless parameter space has been further reduced to fit the scope of the present numerical investigation. A bulk Reynolds number of $Re_b = 6900$ has been chosen for all cases, reducing the flow parameters to only the bulk Mach number, M_b. Preliminary numerical investigations varying the IBCs' undamped resonant angular frequency, ω_r, have led to the discovery that a dramatic flow response is obtained when ω_r is tuned to the characteristic time scale of the large, energy containing eddies in the bulk flow. Based on the normalization adopted in the present work, such tuning condition reads

$$\omega_r = 2\pi M_b. \tag{26}$$

It has been verified that choosing ω_r to be one order of magnitude larger or smaller than (26) (detuning the IBCs) yields no effect on the flow. On the other hand, a very similar response was obtained by choosing $\omega_r = 2\pi M_\infty$ where M_∞ is based on the centerline velocity (instead of bulk velocity), showing the robustness of tuning principle (26).

Tuning the IBCs based on (26) reduces the parameter space to the bulk Mach number, M_b, the damping ratio, ζ, and the resistance, R. A set of three values for each parameter has been chosen in the range

$$\begin{cases} M_b \in \{0.05, & 0.20, & 0.50\}, \\ \zeta \in \{0.50, & 0.70, & 0.90\}, \\ R \in \{0.01, & 0.10, & 1.00\}. \end{cases} \tag{27}$$

Exploring every combination of the aforementioned parameter space has required 27 independent simulations, in addition to 3 baseline runs with no IBCs for each M_b, bringing the overall computational effort up to 30 simulations.

The chosen values for R bracket the value of 0.18 obtained by Tam and Auriault[6] who calibrated the parameters in (15) against the experimentally measured impedance of a typical aeronautical acoustic linear. The Mach number range has been chosen to explore compressibility effects while keeping the computational cost manageable. Values for the damping ratio, ζ, have been chosen to avoid anti-causal IBCs, as discussed in Sec. III A.

The aforementioned LES have been carried out with streamwise and spanwise grid resolutions of $\Delta x^+ < 40$ and $\Delta z^+ < 15$. The superscript, $^+$, indicates quantities in wall-units, measured in our case with respect to $\delta_\nu = (\rho_b u_\tau/\mu_w)^{-1}$ where ρ_b and μ_w are the bulk density and dynamic viscosity at the wall and u_τ is the friction velocity given by

$$u_\tau = \sqrt{\frac{\langle \tau_w \rangle}{\rho_b}}, \tag{28}$$

calculated based on the mean wall-shear stress $\langle \tau_w \rangle$ obtained from the conservation of the integral linear momentum.

The computational domain size has been chosen to properly accommodate the near-wall and outer-layer turbulent structures in the low-Mach-number limit. A sensitivity study to the grid resolution and domain size has been carried out for the $M_b = 0.5$ and $R = 0.01$ case (see Appendix), which, exhibits the strongest response, as discussed in the following.

The governing equations are solved for mass, momentum, and total energy in the finite-volume unstructured code *CharLES*^{X} developed as a joint-effort project among researchers at Stanford University. The flux reconstruction method is grid-adaptive at the preprocessing stage and solution-adaptive at run-time. It blends a high-order flux reconstruction scheme (up to fourth-order accurate on uniform meshes) with a lower-order one ensuring numerical stability in areas of low grid quality.[38] The discretized system of equations is integrated in time with a fully explicit third-order Runge-Kutta scheme. The code is parallelized using the Message Passing Interface (MPI) protocol and highly scalable on a large number of processors. Typical run times for the calculations presented here are of the order of two weeks on approximately two thousand processors per case on a BlueGene Q machine.

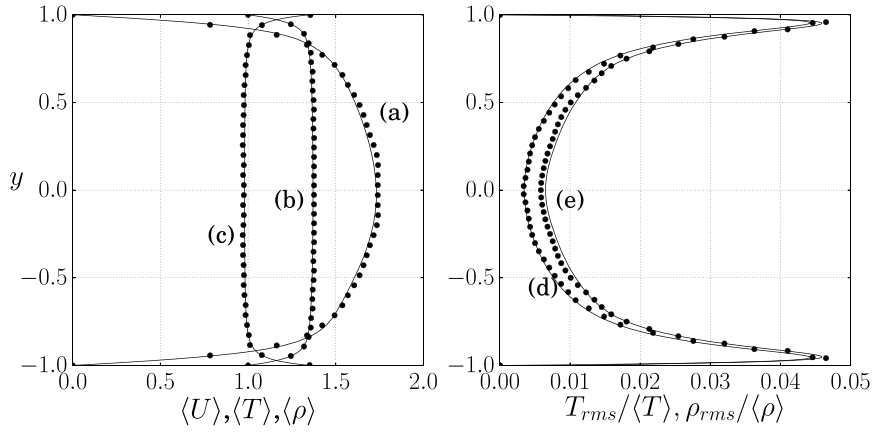

FIG. 4. Comparison between case A in Coleman, Kim, and Moser[31] (•) and a turbulent compressible channel flow at $M_b = 1.5$ with purely reflective IBCs (i.e., residues (9) set to zero) (—). Mean velocity (a), temperature (b), and density (c); root mean square of density (d) and temperature (e) fluctuations normalized with respective local mean values.

IV. COMPRESSIBLE CHANNEL FLOW WITH PURELY REFLECTIVE WALL-IMPEDANCE

In the limit $|Z(\omega)| \to \infty$, reflection coefficient (3) is equal to $\widehat{W}(\omega) = -1$, in which case the IBCs act as a purely reflective (or hard) wall. To verify the correct behavior of the IBCs' implementation in the hard-wall limit, isothermal channel flow results from Coleman, Kim, and Moser[31] have been successfully reproduced (Figure 4) by imposing an infinite wall-impedance, practically obtained by setting the residues in (9) to zero. Results were obtained on a computational domain of $14 \times 2 \times 4$ and a computational grid of $256 \times 192 \times 128$ (respectively, in the streamwise, wall-normal, and spanwise directions) and a minimum wall-normal resolution of $\Delta y = 5 \times 10^{-4}$, based on the channel half-width. The hard-wall behavior can be, in practice, recovered for sufficiently high, but finite, values of $|Z(\omega)|$ (as shown later) and/or by detuning of the IBCs, yielding no structural change to the near-wall turbulence.

V. COMPRESSIBLE CHANNEL FLOW WITH TUNED WALL-IMPEDANCE

A. Tuned wall-impedance

The tuning of IBCs (15) to the characteristic time scale of the energy-containing eddies in bulk flow (26) results in a drag increase, which grows monotonically with the inverse of the resistance, R^{-1}, and/or the bulk Mach number, M_b, exceeding 300% for $M_b = 0.5$ and $R = 0.01$ (Table I, Figure 5). The associated enhancement of the turbulence intensity levels and friction Reynolds number has led to the conservative adoption of a fine computational grid for all the cases investigated (Table II). On the other hand, IBCs with the highest value of resistance, $R = 1.0$ (approaching a hard-wall behavior), allow very limited transpiration through the boundary, leaving the flow structure, hence the drag, unaltered. For any given M_b, a critical value of R^{-1} always exists, at which

TABLE I. Drag increase (%) for different values of ζ and R due to the application of IBCs tuned according to (26) with respect to a baseline case obtained separately for each M_b without IBCs. In all cases, the bulk Reynolds number is fixed at $Re_b = 6900$.

	$M_b = 0.05$			$M_b = 0.2$			$M_b = 0.5$		
	$\zeta = 0.50$	$\zeta = 0.70$	$\zeta = 0.90$	$\zeta = 0.50$	$\zeta = 0.70$	$\zeta = 0.90$	$\zeta = 0.50$	$\zeta = 0.70$	$\zeta = 0.90$
$R = 1.00$	0%	0%	0%	0%	0%	0%	0%	0%	0%
$R = 0.10$	1%	1%	1%	46%	46%	43%	148%	157%	158%
$R = 0.01$	75%	127%	134%	238%	243%	245%	282%	307%	325%

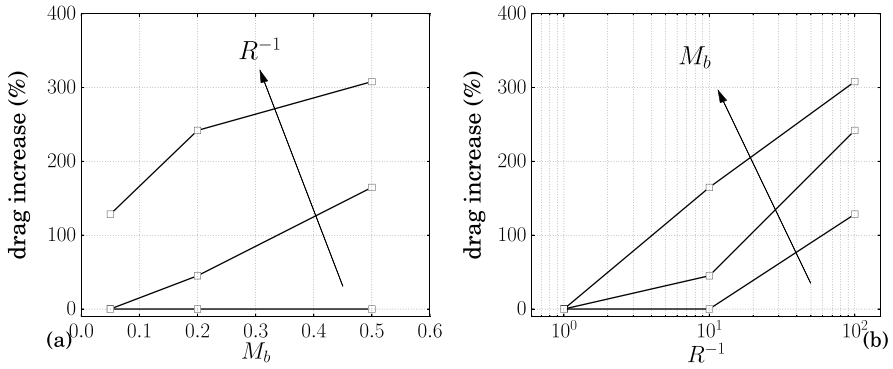

FIG. 5. Drag increase due to the application of IBCs tuned according to (26) with respect to a baseline case obtained separately for each M_b without IBCs. Drag increase (%) versus bulk Mach number, for different values of R^{-1} (a) and versus R^{-1} for different values of M_b (b), averaged over all values of ζ. In all cases, the bulk Reynolds number is fixed at $Re_b = 6900$.

the onset of drag increase occurs (Figure 5(b)). This suggests that, by comparison with previous work on incompressible turbulent flow over porous surfaces,[20] the impedance resistance, R, can be interpreted as the inverse of the wall permeability. This can be argued, in particular, in the case of a turbulent flow interacting with tuned wall-impedance, that is, a flow with temporal spectral energy density concentrated around the IBCs' resonant frequency, ω_r. In this case, impedance (15) can be approximated as

$$R + i\left[\omega X_{+1} - \omega^{-1} X_{-1}\right]\Big|_{\omega \simeq \omega_r} \simeq R, \tag{29}$$

given that

$$\omega_r X_{+1} - \omega_r^{-1} X_{-1} = 0, \tag{30}$$

as per the definition of ω_r (25a). Tuned IBCs can, therefore, be approximately expressed as

$$\hat{v} \simeq R^{-1}\hat{p}, \tag{31}$$

only for the energy-containing modes, $\omega \sim \omega_r$, which justifies the interpretation of R^{-1} as the wall-permeability. Wall-normal modes with frequency much lower, $\omega << \omega_r$, or higher, $\omega >> \omega_r$, than the resonant frequency, ω_r, cause the imaginary part of (15), as well as its absolute value, to diverge. The IBCs, therefore, behave for those modes as purely reflective boundary conditions.

For a given value of the resistance, R, and resonant frequency, ω_r, changes in the damping ratio, ζ (25b), would only alter the absolute values of acoustic stiffness, X_{-1}, and mass, X_{+1}, but not their ratio (25a), therefore, not affecting tuning condition (26) and the considerations leading to (31). The effects of ζ on the flow response (Table I) can, therefore, be regarded as secondary with respect to the tuning and, unless otherwise specified, the following results will only focus on the $\zeta = 0.5$ case.

TABLE II. Streamwise, Δx^+, (minimum) wall-normal Δy^+, and spanwise, Δz^+, resolution in wall units for all combinations of $M_b = \{0.05, 0.2, 0.5\}$ and $R = \{0.01, 0.10, 1.00\}$. Values reported for each M_b and R are the maximum among all values of ζ. All cases have been run on a computational domain of size $6\times2\times6$. See Appendix for sensitivity analysis to the box size and grid resolution.

	$M_b = 0.05$			$M_b = 0.2$			$M_b = 0.5$		
	Δx^+	Δy^+	Δz^+	Δx^+	Δy^+	Δz^+	Δx^+	Δy^+	Δz^+
$R = 1.00$	17.3	0.4	6.9	17.2	0.4	6.9	17.0	0.4	6.8
$R = 0.10$	17.6	0.4	7.0	20.9	0.4	8.4	27.7	0.6	21.6
$R = 0.01$	26.3	0.6	10.5	32.2	0.7	12.9	35.0	0.7	26.4

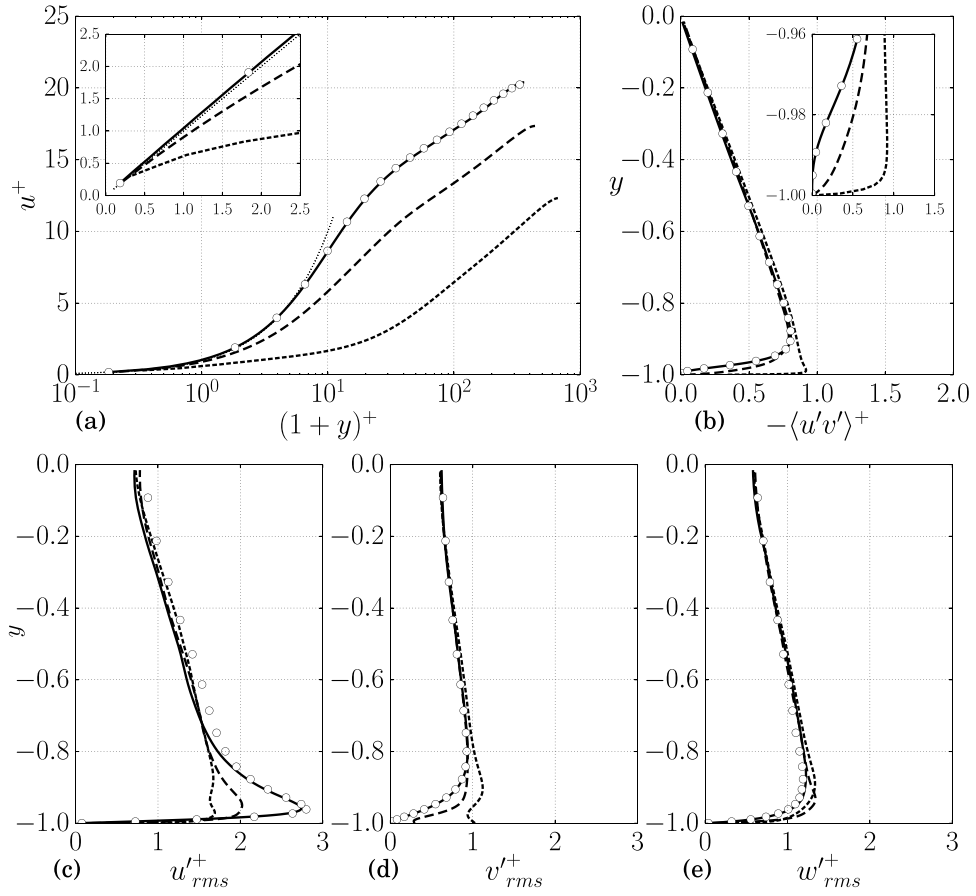

FIG. 6. Profiles of mean streamwise velocity (a), resolved Reynolds shear stress (b), and velocity RMS (c), (d), (e) for $M_b = 0.2$ and $\zeta = 0.5$. Hard-wall case (without IBCs) plotted every 8 points (∘) and with IBC for $R = 1.00$ (—), $R = 0.10$ (– –) and $R = 0.01$ (- - -). Law of the wall $u^+ = y^+$ (···) in (a). The fluctuation intensity of the wall-normal velocity at the boundary is $v'^+_{rms} = 0.01$ for $R = 1.00$.

B. Turbulent statistics

The onset of drag increase is associated with a complete reorganization of the buffer-layer turbulence. Consistently with the considerations leading to (31), lowering the resistance intensifies the magnitude of the wall-normal transpiration (Figure 6(d)), extending the influence of the tuned IBCs further into the channel core. The non-zero limiting behavior of the Reynolds shear-stress gradient at the wall (Figure 6(b), inset) is responsible for the deviations from the law of the wall of the mean streamwise velocity profiles (Figure 6(a)). This effect was not evident, for example, in the incompressible calculations of Jiménez *et al.*[20] due to the relatively low permeabilities tested, corresponding, at most, to $R^{-1} = 14$, for the present $M_b = 0.05$ case. Variations in the log-law's slope are not significant, indicating a substantially unaltered turbulent kinetic energy balance in the outer logarithmic layer[24] (unaltered Kármán constant), with changes in the intercept value merely due to the increased frictional velocity. As shown later, the structure of the outer-layer turbulence is not affected by the application of the tuned IBCs.

As the IBC resistance is relaxed, the near-wall RMS streamwise velocity distribution plateaus (Figure 6(c)) while decreasing in value if normalized with friction velocity (28). The disappearance of the RMS peak suggests that new near-wall turbulent production dynamics are established (as shown later). On the other hand, the wall-normal (Figure 6(d)) and spanwise (Figure 6(e)) velocity RMS in wall-units increase with R^{-1}, the former reaching unity at the wall for $R = 0.01$, for all M_b investigated.

The effects on the mean and RMS velocity profiles are qualitatively consistent with the incompressible simulations by Jiménez *et al.*,[20] suggesting, as anticipated in Sec. V A, that tuned IBCs are akin to porous-wall boundary conditions. However, while in the present cases, structural flow changes are confined to the near-wall region, Jiménez *et al.*[20] observed the formation of large, spanwise coherent rollers only in the core of the channel, with size comparable to the computational domain, modulating unaltered near-wall turbulence.

Spatial correlations have been evaluated to analyze the turbulent flow structure under the effects of tuned IBC. Two-point spatial autocorrelations in the streamwise and spanwise directions for a generic fluctuating quantity, ϕ', have been computed, respectively, as

$$R_{\phi\phi}(\Delta x; y) = \frac{\langle \phi'(x, y, z, t)\phi'(x + \Delta x, y, z, t)\rangle}{\phi'^2_{\text{rms}}(y)} \tag{32}$$

and

$$R_{\phi\phi}(\Delta z; y) = \frac{\langle \phi'(x, y, z, t)\phi'(x, y, z + \Delta z, t)\rangle}{\phi'^2_{\text{rms}}(y)}, \tag{33}$$

where $\langle\cdot\rangle$ represents the averaging operator over the directions of statistical homogeneity (x, z, and t) and $\phi'^2_{\text{rms}}(y)$ the variance at a given y-location. Such correlations computed for the velocity and pressure fields (Figure 7) confirm that the effects of tuned IBCs are confined to the near-wall region, consistently with the results shown in Figure 6.

A well-defined spatially periodic structure emerges, noticeable especially in the autocorrelations $R_{vv}(\Delta x)$ and $R_{pp}(\Delta x)$, and also, less clearly, in $R_{uu}(\Delta x)$ and $R_{ww}(\Delta x)$, with an overall significant shortening of the streamwise turbulent integral length scales. The strong periodic signature shared by R_{vv} and R_{pp} suggests the presence of a flow instability composed of predominantly wall-normal acoustic modes, which are confined in a layer close to the impedance wall. These occur, in fact, at the tuned IBCs undamped resonant frequency,

$$f_r = \omega_r/2\pi = M_b \tag{34}$$

as confirmed by one-point time autocorrelations, such as

$$R_{vv}(\Delta\tau; y) = \frac{\langle v'(x, y, z, t)v'(x, y, z, t + \Delta\tau)\rangle}{v'^2_{\text{rms}}(y)}, \tag{35}$$

shown in Figure 8. This result is consistent with the analysis in Sec. V A showing that wall-normal transpiration is associated only with modes exciting the wall-impedance at (or close to) its undamped resonant frequency, ω_r. The finite thickness of the layer where such resonant modes are trapped, taking on most of the local turbulent kinetic energy production (discussed later), its wave-like properties and the fact that it separates an outer logarithmic layer from an extremely thin viscous region, has led to its designation as *resonance buffer layer*. The objective of the remainder of the manuscript is to characterize its properties.

C. Resonance buffer layer

The absence of a spanwise periodic signature in the spatial auto-correlations (Figure 7, right) suggests a two-dimensional structure for the observed instability. The streamwise wavelength, λ_x (Figure 9), shows no appreciable variation with y or M_b, despite the significant variations in friction Reynolds numbers from $M_b = 0.05$ to $M_b = 0.5$. Its average value of $\lambda_x = 0.4$ corresponds exactly to $\lambda_x = 1/15\ L_x$, where L_x is the streamwise extent of the computational domain. A sensitivity analysis to the computational domain size and grid resolution (Appendix) confirms that the observed flow response is not an artifact of the particular numerical setup, with the caveat of λ_x being necessarily an integer fraction of L_x.

A fully developed resonance buffer layer is established after approximately 5-10 flow-through times from the application of the tuned IBCs. Spanwise autocorrelations of wall-normal velocity fluctuations, $R_{vv}(\Delta z)$, and streamwise velocity fluctuations, $R_{uu}(\Delta z)$, reveal no trace of the typical buffer layer turbulent structures responsible for sustaining the smooth-wall turbulence production

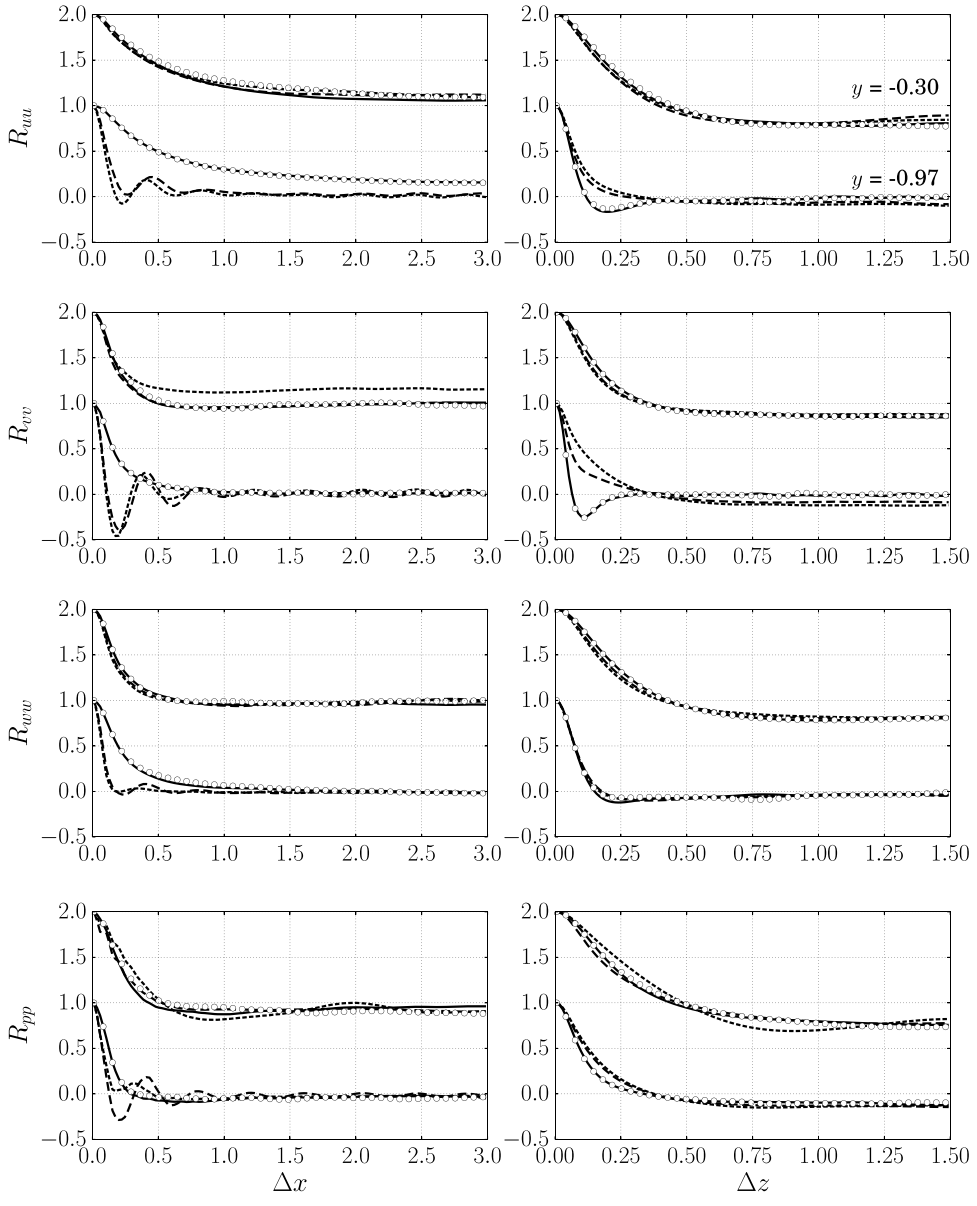

FIG. 7. Streamwise (left) and spanwise (right) two-point autocorrelations for $M_b = 0.5$. Hard walls (no IBCs) (∘), with IBCs for $R = 1.00$ (—), $R = 0.10$ (– –), and $R = 0.01$ (- - -) for $\zeta = 0.5$, at $y = -0.97$ and $y = -0.30$ (shifted by +1).

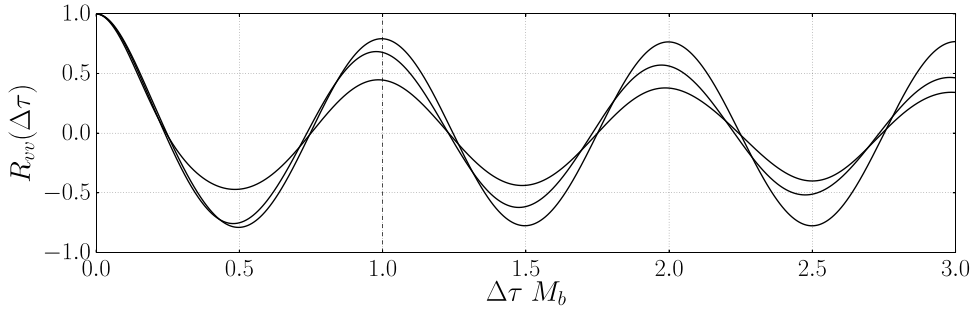

FIG. 8. Temporal autocorrelations of wall-normal velocity fluctuations for $M_b = 0.05$, $M_b = 0.20$, and $M_b = 0.5$ at $y = -0.98$. Vertical dashed line indicates the time separation corresponding to the tuned frequency $\Delta\tau = f_r^{-1} = M_b^{-1}$.

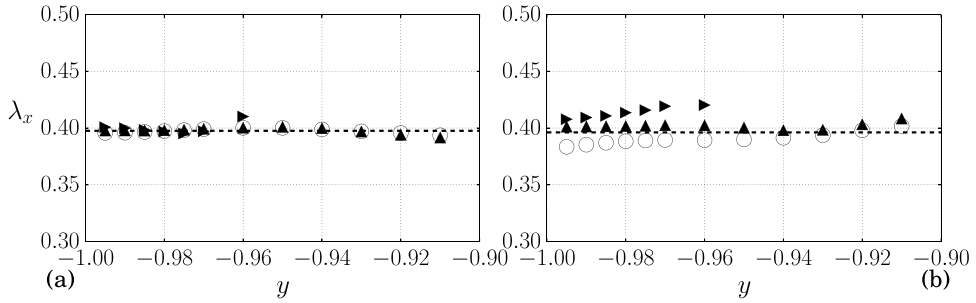

FIG. 9. Wall-normal distribution of streamwise wavelength, λ_x, estimated from autocorrelations $R_{uu}(\Delta x)$ (►), $R_{vv}(\Delta x)$ (▲), $R_{pp}(\Delta x)$ (○) for $M_b = 0.05$ (a) and $M_b = 0.5$ (b) for $\zeta = 0.5$ and $R = 0.10$. Average value $\lambda_x \simeq 0.40$ (- - -), corresponding to mode $\lambda_x = 1/15\, L_x$, where L_x is the streamwise extent of the computational domain. Same result obtained for $M_b = 0.2$ (not shown).

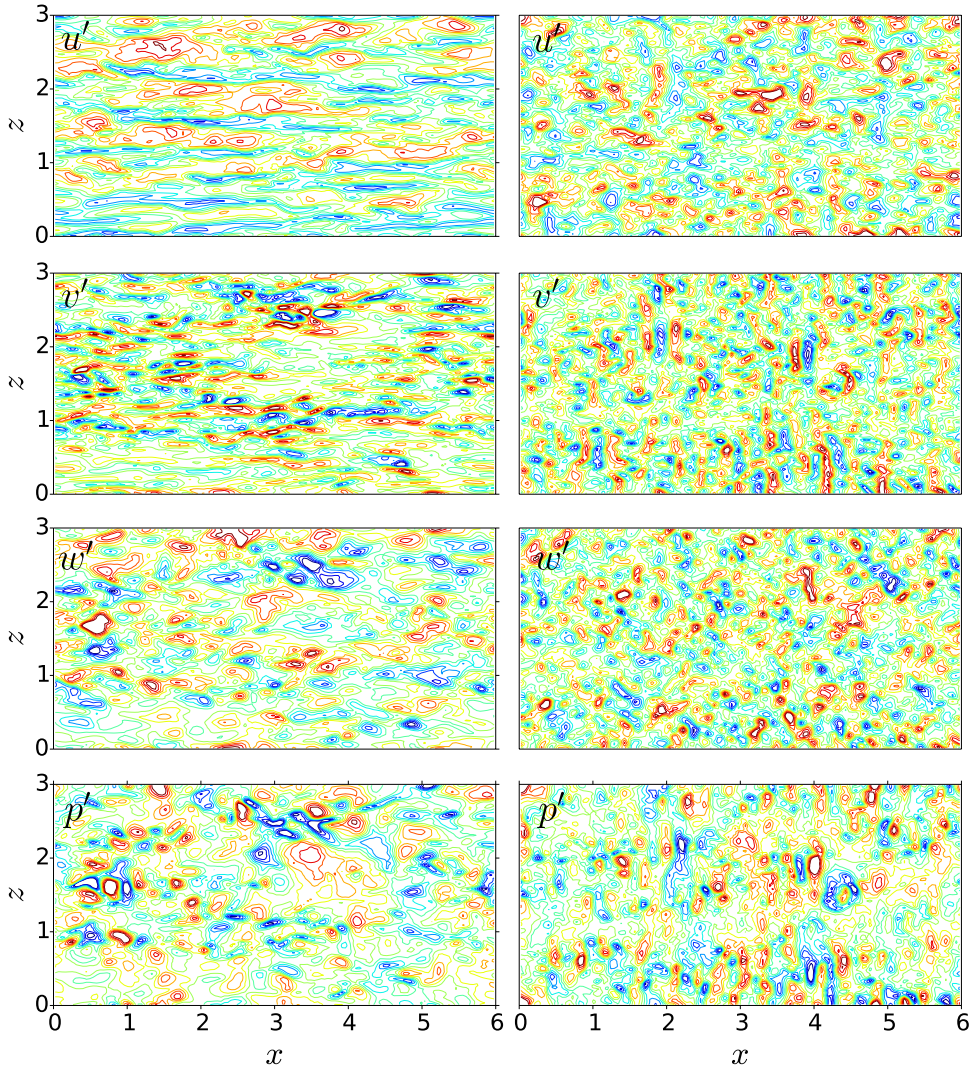

FIG. 10. Contours of instantaneous velocity and pressure fluctuations at $y = -0.95$ for $M_b = 0.5$, without IBC (left) and with tuned IBCs (right) for $R = 0.01$ and $\zeta = 0.5$. The color levels on each plot have been adjusted based on $\pm 5\sigma$ where σ is the standard deviation of each plotted quantity.

cycle.[21] Instantaneous visualizations reveal a complete re-alignment of the near-wall turbulent coherent structures (Figure 10) and, therefore, a necessary reorganization of the associated turbulent production dynamics. The weaker periodic signature in $R_{uu}(\Delta x)$ and $R_{ww}(\Delta x)$ suggests that streamwise and spanwise velocity fluctuations do not play a primary role in the sustainment of the observed flow instability.

In the incompressible calculations by Jiménez *et al.*,[20] the preferred streamwise wavelength of the instability was $\lambda_x \simeq 5$, comparable to the computational domain size. Alterations to the flow were manifest in the form of large rollers in the outer layer responsible for modulating near-wall turbulence with extended regions of almost uniform suction or blowing, as in the numerical experiments by Sumitani and Kasagi.[39] The instability observed in the present calculations exhibits similar characteristics (discussed below), with fundamental differences including the fact that it completely replaces the previously present near-wall turbulent state (rather than simply modulating it), is confined in a well-defined layer near the wall and is not purely hydrodynamic.

Visual inspection of three-dimensional flow structures in the resonance buffer layer (Figure 11) reveals a streamwise-periodic array of spanwise-coherent Kelvin-Helmholtz rollers traveling in the downstream direction. It is therefore possible to assume that

$$\tilde{v}'(x,t) = \mathcal{F}\left(2\pi\left[\frac{x}{\lambda_x} - f_r\, t\right]\right) = \mathcal{F}\left(\frac{2\pi}{\lambda_x}\left[x - c_x\, t\right]\right), \tag{36}$$

where $\tilde{v}'(x,t)$ is the coherent component of the wall-normal velocity fluctuations at any given y location within the resonance buffer layer and $\mathcal{F}(\cdot)$ is a generic periodic function with fundamental period 2π. For a given frequency, f_r (Figure 8), and streamwise wavelength, λ_x (Figure 9), the wave-propagation speed, c_x, in (36) is kinematically constrained to be

$$c_x = \lambda_x\, f_r = \lambda_x\, M_b, \tag{37}$$

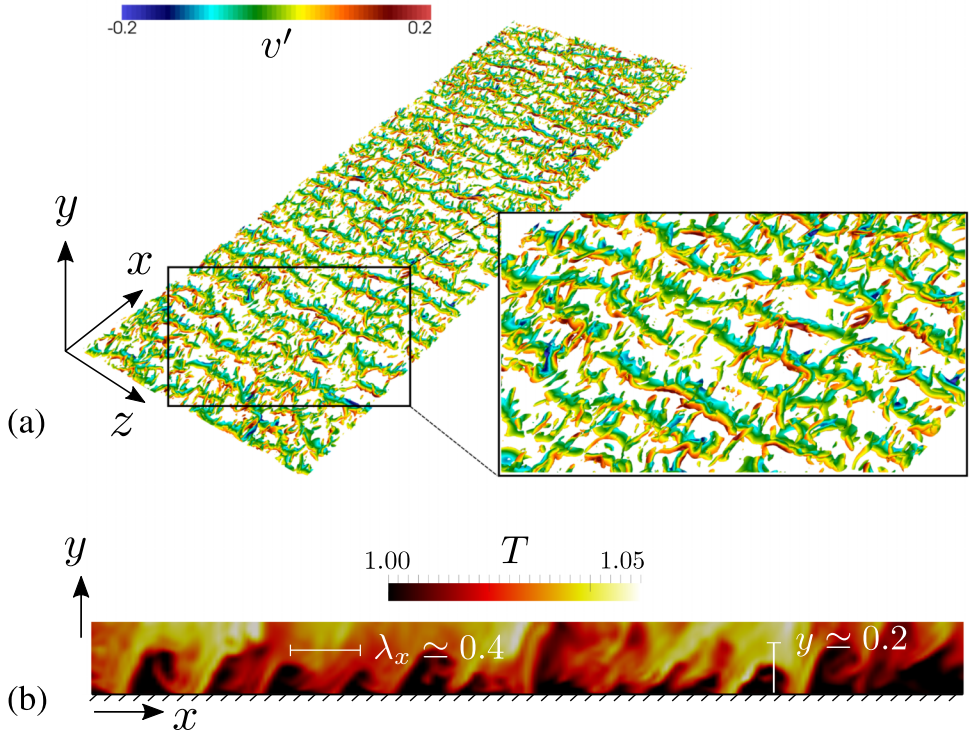

FIG. 11. Isosurfaces of second velocity gradient invariant $Q = 5.0$ colored by vertical velocity fluctuations showing hydroacoustic instability within the resonance buffer layer for $M_b = 0.5$, $R = 0.01$, $\zeta = 0.5$ (a), vertical slice of instantaneous temperature contours with approximate streamwise wavelength, λ_x, and height of the resonance buffer layer (b). Results obtained on computational domain size $12\times2\times6$ with resolution doubled in every direction with respect to Table II.

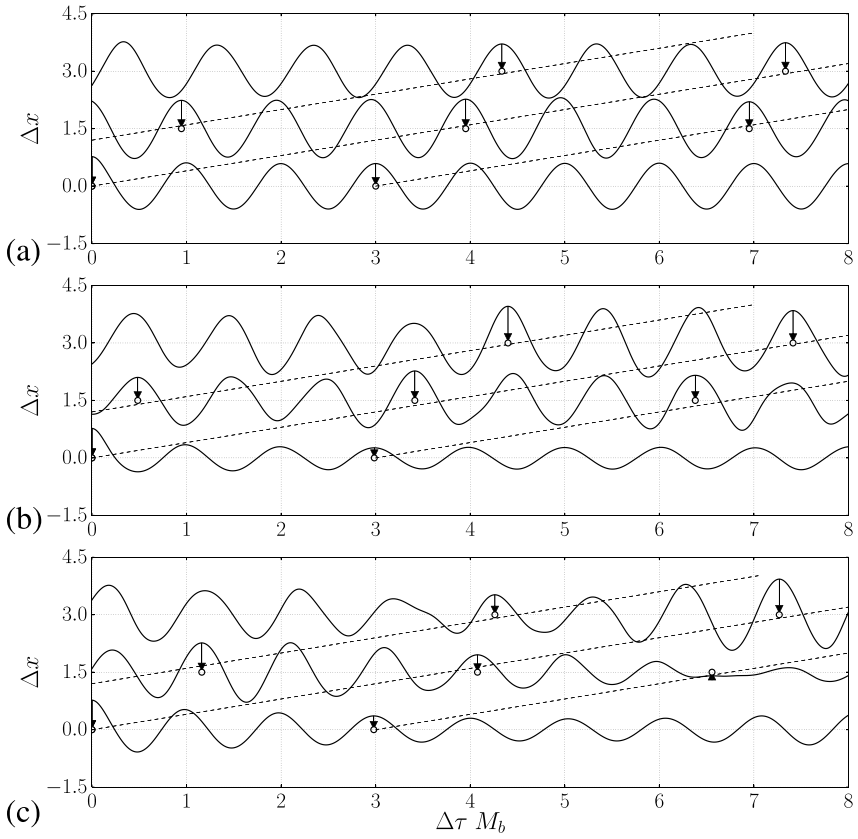

FIG. 12. Space-time correlation (38) for $M_b = 0.05$ (a), $M_b = 0.20$ (b), $M_b = 0.5$ (c) at $y = -0.98$ plotted against the Mach-number-scaled time separation $\Delta\tau\, M_b$ and shifted upwards by the separation distance Δx. The wave propagation speed predicted by (39) is shown by dashed lines.

where the (non-dimensionalized) resonant frequency, f_r, is equal to the bulk Mach number, based on tuning condition (34). Two-point space-time autocorrelations of wall-normal velocity fluctuations,

$$R_{vv}(\Delta x, \Delta\tau; y) = \frac{\langle v'(x,y,z,t)v'(x+\Delta x, y, z, t+\Delta\tau)\rangle}{v'^2_{\text{rms}}} \tag{38}$$

(Figure 12), confirm the value of the wave-speed predicted in (37). The propagation speed of the correlation peak occurs, in fact, at

$$\frac{\Delta x}{\Delta\tau} = c_x = \lambda_x M_b. \tag{39}$$

While the advection velocity of the instability observed by Jiménez *et al.*[20] is argued to scale in wall units, the result in (37) does not suggest any dependency of c_x from viscous parameters being λ_x a constant value for all the cases investigated (Figure 9), therefore supporting the inviscid nature of the instability.

The degree of temporal and spatial coherence of the resonance buffer layer structures is such that no triple decomposition via spanwise averaging or phase locking of instantaneous quantities is necessary to compute statistics, especially for the lower Mach number cases (lower turbulence intensity levels).

Overall, the flow dynamics of the resonance buffer layer display all of the key features of an inviscid Kelvin-Helmholtz instability. Such hydrodynamic instability is, however, driven by the wall-normal wave propagation resulting from resonant excitation of the tuned IBCs (as discussed in Sec. V A), therefore leading to the designation of hydro-acoustic instability. This type of instability

was theoretically predicted by Rienstra and co-workers[8–10] and experimentally identified in few previous works[11] in analogous flow configurations.

The signature of the spanwise rollers in the resonance buffer layer is evident in the excess Reynolds shear stresses detected in the near-wall region (Figure 6(b), inset). Moreover, the wall-normal transpiration is responsible for the non-zero Reynolds shear stress gradient at the wall, preventing the formation of a purely viscous sublayer. This results in a shift of the turbulent energy production peak (not shown) towards a location very close to the wall, causing the extreme thinning of the viscous sublayer, experiencing up to an order of magnitude decrease in thickness (Figure 6(b), inset). The frictional drag increase can be straightforwardly understood within the context of the surface renewal theory,[40–43] which quantitatively links the intensification of near-wall convective events (such as bursts and ejections, traditionally) to the thinning of the viscous sublayer and, hence, the enhancement of the turbulent momentum transfer at the wall.

A different structure of the flow instability is present in the incompressible calculations by Jiménez *et al.*[20] The observed flow instability is associated with a very large scale outer layer rollers modulating otherwise unaltered buffer-layer turbulence. The excess drag was attributed to the wall-friction increase in regions of suction, outweighing the wall-friction decrease in regions of blowing. Moreover, in Jiménez *et al.*'s[20] calculations, even at the highest porosities investigated, near-wall turbulent production mechanisms were not affected, while, in the present case, even for $M_b = 0.05$ (approaching the incompressible limit), near-wall turbulence is completely redefined, overhauled by the newly established resonance buffer layer.

VI. CONCLUSIONS

We have investigated the possibility of passively controlling a compressible turbulent flow with the application of IBCs. The latter are chosen as a three-parameter damped Helmholtz oscillator with resonant frequency tuned to the characteristic time scale of the outer-layer eddies, taken as the ratio of the bulk velocity over the boundary-layer thickness. By fixing the bulk Reynolds number to $Re_b = 6900$, the degrees of freedom of the overall dimensionless parameter space to explore are reduced to three: the bulk Mach number, M_b, the IBCs' damping ratio, ζ, and resistance, R. A total of 27 LES have been carried out to explore all possible combinations of three bulk Mach numbers ($M_b = 0.05, 0.2, 0.5$), three damping ratios ($\zeta = 0.5, 0.7, 0.9$), and three resistances ($R = 0.01, 0.10, 1.00$). Three additional LES with isothermal walls were performed at each Mach number to serve as reference simulations for analysis and comparison. One direct numerical simulation was also performed with IBCs in the limit of zero wall-softness (or $|Z(\omega)| \to \infty$), successfully reproducing the $M_b = 1.5$ isothermal wall calculations by Coleman, Kim, and Moser.[31] The IBCs have been formulated in the time domain according to Fung and Ju[1] and coupled with a fully explicit compressible Navier-Stokes solver. Excellent agreement is obtained with semi-analytical solutions derived assuming linear acoustics. The adopted numerical coupling strategy is spatially and temporally consistent, it can be straightforwardly implemented within the framework of higher-order numerics and extended to account for grazing flow effects.

At sufficiently high Mach numbers, M_b, and/or low resistances, R, the application of tuned IBCs generates strong hydro-acoustic instabilities. They are confined in the resonance buffer layer and appear in the form of a streamwise-periodic array of spanwise-coherent Kelvin-Helmholtz rollers, completely replacing classic buffer-layer turbulent coherent structures. Such large-scale vortical structures remain confined near the wall and travel downstream with advection velocity $c_x = \lambda_x f_r$, where λ_x is the average distance between two adjacent rollers and $f_r = M_b$ is the (dimensionless) tuned resonant frequency. The advection velocity is, therefore, a function of the streamwise extent of the computational domain L_x, being λ_x necessarily an integer fraction of L_x. The hydrodynamic instability responsible for the generation of the Kelvin-Helmholtz rollers is triggered by the interaction between the background mean velocity gradient and high-amplitude wall-normal propagating waves at the frequency f_r. The latter result, in turn, from resonant excitation of the tuned IBCs and are evanescent in the outer layer. The alteration of the near-wall turbulent structure leads to a significant increase in the Reynolds shear stress near the wall. In particular,

the value of the Reynolds shear stress gradient near the wall is non-zero, resulting in a departure of the mean velocity profiles from the law of the wall, while all statistical quantities in the outer layer collapse for all R's investigated if normalized by friction velocity. The mean velocity profiles in the outer region preserve a logarithmic behavior in all cases. This shows that the resonance buffer layer is confined near the wall by structurally unaltered outer-layer equilibrium turbulence. No quantitative differences in the drag increase and in the altered turbulent structure are observed by changing the grid resolution and/or the domain size for the highest Mach number case and the lowest value of the resistance.

A systematic investigation at higher Mach numbers will be pursued in future studies. Preliminary results show that the flow response is further amplified, consistently with the trends predicted in the present manuscript. Extreme thinning of the viscous and thermal sublayers is observed for $M_b > 0.5$ for the range of resistances investigated, making grid resolution an issue. Moreover, the intensified transpiration at the boundary also calls into question the validity of a linear model for the wall impedance,[44] especially at higher Mach numbers.

The strong flow response observed in the present study suggests that the proposed computational strategy can be successfully employed in modeling passive flow control devices with a well-defined acoustic response. Possible applications include enhancement of turbulent heat and mass transfer, delaying transonic boundary-layer separation, and/or controlling second-mode instabilities in transitional hypersonic boundary layers. Acoustically tunable porous surfaces can be designed building upon traditional acoustic liners by tweaking two simple features: the size of the Helmholtz cavities can, in fact, be adjusted to resonate at the characteristic time scales of the flow, following (26); the porosity of the surface coatings and orifice sizes can be adjusted to achieve the desired permeability. Simple parametrizations such as the ones provided in Chanaud[45] can be used to relate the characteristic resonant frequency (controlled by the imaginary part of the impedance in (15)) with all the geometrical features of the resonator, including the orifice size. The latter also regulates the effective surface permeability, inversely proportional to the impedance resistance in (15). This flow control strategy has been already successfully adopted by Yang and Spedding[12] to control laminar boundary layer separation over an Eppler 387 wing.

ACKNOWLEDGMENTS

The authors would like to thank Professor Laurent Joly for providing feedback on the entire manuscript, for suggestions on the analysis of the near-wall vortical structure, the review of previous work on the topic and overall enabling cross-pollination of ideas on the matter. Carlo Scalo would like to thank Professor Dr. Jan Werner Delfs for the useful discussions (on an unrelated project) that have inspired the idea of tuned impedance boundary conditions and Dr. Qiqi Wang for the discussions over the Mach number scaling of the drag increase. The computational resources were provided by CNRS on the BlueGene Q system Turing thanks to the GENCI-IDRIS Grant No. x20142a7178 as well as the support provided by Purdue by allowing early access to Conte, the newest of Purdue's Community Clusters.

APPENDIX: SENSITIVITY TO BOX SIZE AND GRID RESOLUTION

The computational domain size ($6 \times 2 \times 3$) and resolution (see Table II) adopted for the complete set of 30 large-eddy simulations have been chosen to properly accommodate and resolve the near-wall and outer layer structures only in the low-Mach number limit and for smooth walls. It is, therefore, necessary to verify whether the observed flow response might be an artifact of the specific computational domain size and grid resolution adopted, especially for the higher Mach number case. This section will explore the aforementioned issues by focusing on the case, $M_b = 0.5$, $\zeta = 0.5$, $R = 0.01$, exhibiting strongest flow response.

Most of the spanwise autocorrelations in Figure 7 are not completely vanishing asymptotically, while the only streamwise correlations that might raise some concerns are $R_{uu}(\Delta x)$ and $R_{vv}(\Delta x)$ near the centerline. To address these issues, the case for $M_b = 0.5$, $\zeta = 0.5$, $R = 0.01$ has been first run on a computational domain doubled in size both in the spanwise z, and streamwise directions x,

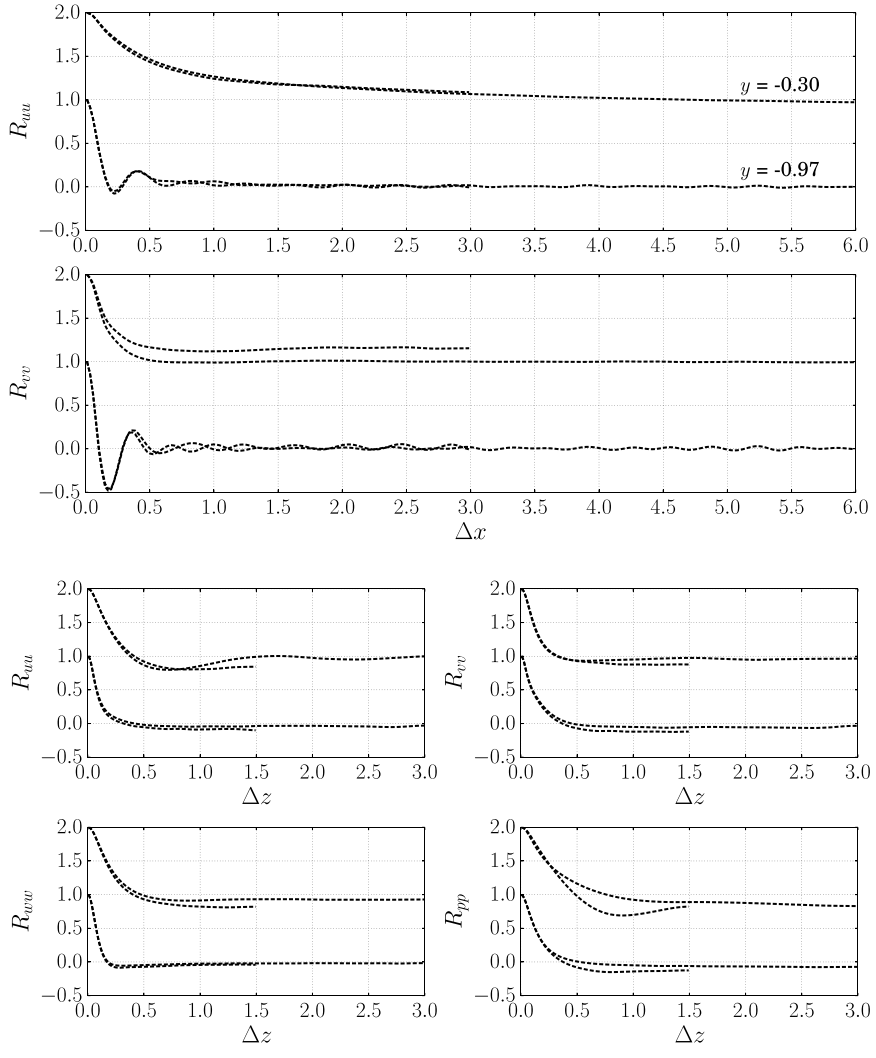

FIG. 13. Selected autocorrelations for $M_b = 0.5$, $R = 0.01$, $\zeta = 0.5$ for computational domain size $6\times2\times3$ and $12\times2\times6$, both at the same resolution reported in Table II, at $y = -0.97$ and $y = -0.30$ (shifted by +1).

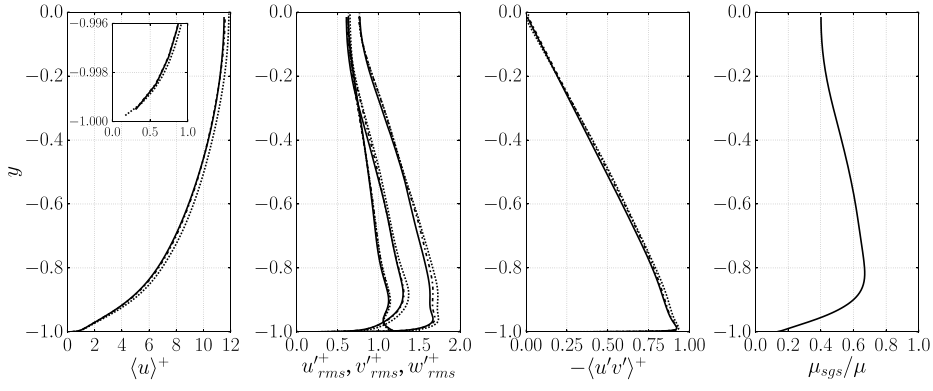

FIG. 14. Effect of computational domain size and grid resolution for case $M_b = 0.5$, $R = 0.01$, $\zeta = 0.5$ on the average streamwise velocity $\langle u\rangle^+$, standard deviations u^+_{rms}, v^+_{rms}, w^+_{rms}, and Reynolds shear stresses, $\langle u'v'\rangle^+$. Computational domain size $6\times2\times3$ with resolution given in Table II (—), domain size $12\times2\times6$, same resolution (-··-) and domain size $12\times2\times6$ with resolution doubled in every direction (···). Resulting friction velocity $u_\tau/U_b = 0.114$, 0.113, and 0.110, respectively. Subgrid-scale eddy viscosity μ_{sgs} normalized with molecular viscosity μ is shown for one case only.

retaining the same spatial resolution (i.e., doubling the number of grid points). The resolution has then been doubled in x and z while retaining the larger computational domain.

A negligible difference is observable in the statistics and drag increase (Figures 13 and 14), with changes in friction velocity within statistical uncertainty. The maximum value of the ratio of the subgrid scale eddy viscosity to the molecular one is reduced from 0.64 to 0.30 after one refinement step. The simulation with a higher resolution predicts higher velocity RMS values, as expected.

[1] K. Y. Fung and H. Ju, "Time-domain impedance boundary conditions for computational acoustics and aeroacoustics," Int. J. Comput. Fluid Dyn. **18**, 503–511 (2004).
[2] S. W. Rienstra, "Impedance models in time domain, including the extended Helmholtz resonator model," AIAA Paper 2006-2686, 2006.
[3] C. Richter, J. Abdel-Hay, L. Panek, N. Schonwald, S. Busse, and F. Thiele, "Time domain impedance modelling and applications," Procedia Eng. **6**, 133–142 (2010).
[4] Y. Özyörük and L. N. Long, "A time-domain implementation of surface acoustic impedance condition with and without flow," J. Comput. Acoust. **5**, 277–296 (1997).
[5] Y. Özyörük, L. N. Long, and M. G. Jones, "Time-domain numerical simulation of a flow-impedance tube," J. Comput. Phys. **146**, 29–57 (1998).
[6] C. K. W. Tam and L. Auriault, "Time-domain impedance boundary conditions for computational aeroacoustics," AIAA J. **34**, 917–923 (1996).
[7] C. K. W. Tam, "Advances in numerical boundary conditions for computational aeroacoustics," J. Comput. Acoust. **6**, 377–402 (1998).
[8] S. W. Rienstra and G. G. Vilenski, "Spatial instability of boundary layer along impedance wall," AIAA Paper 2008-2932, 2008.
[9] S. W. Rienstra and M. Darau, "Boundary-layer thickness effects of the hydrodynamic instabilty along an impedance wall," J. Fluid Mech. **671**, 559–573 (2011).
[10] G. G. Vilenski and S. W. Rienstra, "On hydrodynamic and acoustic modes in a ducted shear flow with wall lining," J. Fluid Mech. **583**, 45–70 (2007).
[11] G. Boyer, E. Piot, and J. Brazier, "Numerical study of hydrodynamic unstable modes in a ducted shear flow with wall lining and comparison to experiments," AIAA Paper 2010-3943, 2010.
[12] S. L. Yang and G. R. Spedding, "Passive separation control by acoustic resonance," Exp. Fluids **54**, 1603 (2013).
[13] Q. Zhang and D. J. Bodony, "Numerical simulation of two-dimensional acoustic liners with high-speed grazing flow," AIAA J. **49**, 365–382 (2011).
[14] C. Ostoich, D. J. Bodony, and P. H. Geubelle, "Interaction of a Mach 2.25 turbulent boundary layer with a fluttering panel using direct numerical simulation," Phys. Fluids **25**, 110806 (2013).
[15] C. K. Tam, N. Pastouchenko, M. G. Jones, and W. R. Watson, "Experimental validation of numerical simulation for an acoustic liner in grazing flow," AIAA Paper 2013-2222, 2013.
[16] A. Wagner, K. Hannemann, and M. Kuhn, "Ultrasonic absorption characteristics of porous carbon–carbon ceramics with random microstructure for passive hypersonic boundary layer transition control," Exp. Fluids **55**, 1750 (2014).
[17] G. A. Bres, M. Inkman, T. Colonius, and A. V. Fedorov, "Second-mode attenuation and cancellation by porous coatings in a high-speed boundary layer," J. Fluid Mech. **726**, 312 (2013).
[18] N. De Tullio and N. D. Sandham, "Direct numerical simulation of breakdown to turbulence in a Mach 6 boundary layer over a porous surface," Phys. Fluids **22**, 094105 (2010).
[19] V. Wartemann, H. Lüdeke, and N. D. Sandham, "Numerical investigation of hypersonic boundary-layer stabilization by porous surfaces," AIAA J. **50**, 1281 (2012).
[20] J. Jiménez, M. Uhlmann, A. Pinelli, and G. Kawahara, "Turbulent shear flow over active and passive porous surfaces," J. Fluid Mech. **442**, 89–117 (2001).
[21] J. Jiménez and A. Pinelli, "The autonomous cycle of near-wall turbulence," J. Fluid Mech. **389**, 335–359 (1999).
[22] O. Flores and J. Jiménez, "Effect of wall-boundary disturbances on turbulent channel flows," J. Fluid Mech. **566**, 357–376 (2006).
[23] J. Jiménez, "Turbulent flows over rough walls," Annu. Rev. Fluid Mech. **36**, 173–196 (2004).
[24] A. Townsend, *The Structure of Turbulent Shear Flows* (Cambridge University Press, 1976).
[25] J. Yuan and U. Piomelli, "Numerical simulations of sink-flow boundary layers over rough surfaces," Phys. Fluids **26**, 015113 (2014).
[26] D. S. Henn and R. I. Sykes, "Large-eddy simulation of flow over wavy surfaces," J. Fluid Mech. **383**, 75–112 (1999).
[27] K. Frederick and T. Hanratty, "Velocity measurements for a turbulent nonseparated flow over solid waves," Exp. Fluids **6**, 477–486 (1988).
[28] A. Zenklusen, S. Kuhn, and P. R. Von Rohr, "Structural dissimilarity of large-scale structures in turbulent flows over wavy walls," Phys. Fluid **24**, 055112 (2012).
[29] R. Garcia-Mayoral and J. Jiménez, "Hydrodynamic stability and breakdown of the viscous regime over riblets," J. Fluid Mech. **678**, 317–347 (2011).
[30] P. G. Huang, G. N. Coleman, and P. Bradshaw, "Compressible turbulent channel flows: DNS results and modelling," J. Fluid Mech. **305**, 185–218 (1995).
[31] G. N. Coleman, J. Kim, and R. D. Moser, "A numerical study of turbulent supersonic isothermal-wall channel flow," J. Fluid Mech. **305**, 159–183 (1995).
[32] R. Lechner, J. Sesterhenn, and R. Friedrich, "Turbulent supersonic channel flow," J. Turbul. **2**, N1 (2001).

[33] H. Foysi, S. Sarkar, and R. Friedrich, "Compressibility effects and turbulence scalings in supersonic channel flow," J. Fluid Mech. **509**, 207–216 (2004).
[34] S. Ghosh, H. Foysi, and R. Friedrich, "Compressible turbulent channel and pipe flow: Similarities and differences," J. Fluid Mech. **648**, 155–181 (2010).
[35] A. Leonard, "Energy cascade in large-eddy simulations of turbulent fluid flows," Adv. Geophys. **18**, 237–248 (1974).
[36] A. W. Vreman, "An eddy-viscosity subgrid-scale model for turbulent shear flow: Algebraic theory and applications," Phys. Fluids **16**, 3670 (2004).
[37] D. Y. Shang and B. X. Wang, "Effect of variable thermophysical properties on laminar free convection of gas," Int. J. Heat Mass Transfer **33**, 1387–1395 (1990).
[38] F. Ham, K. Mattsson, G. Iaccarino, and P. Moin, *Towards Time-Stable and Accurate LES on Unstructured Grids* (Springer, Berlin, Heidelberg, 2007), pp. 235–249.
[39] Y. Sumitani and N. Kasagi, "Direct numerical simulation of turbulent transport with uniform wall injection and suction," AIAA J. **33**, 1220–1228 (1995).
[40] W. Pinczewski and S. Sideman, "A model for mass (heat) transfer in turbulent tube flow. Moderate and high Schmidt (Prandtl) numbers," Chem. Eng. Sci. **29**, 1969–1976 (1974).
[41] T. J. Hanratty, "Turbulent exchange of mass and momentum with a boundary," AIChE J. **2**, 359–362 (1956).
[42] K. K. Sirkar and T. J. Hanratty, "Relation of turbulent mass transfer to a wall at high Schmidt numbers to the velocity field," J. Fluid Mech. **44**, 589–603 (1970).
[43] C. Scalo, U. Piomelli, and L. Boegman, "High-Schmidt-number mass transport mechanisms from a turbulent flow to absorbing sediments," Phys. Fluids **24**, 085103 (2012).
[44] Q. Zhang and D. J. Bodony, "Numerical investigation and modeling of acoustically-excited flow through a circular orifice backed by a hexagonal cavity," J. Fluid Mech. **693**, 367–401 (2012).
[45] R. Chanaud, "Effects of geometry on the resonance frequency of Helmholtz resonators," J. Sound Vib. **178**, 337–348 (1994).